

IRAS PSCZ V.S. IRAS 1.2-JY MODEL VELOCITY FIELDS: A SPHERICAL HARMONICS COMPARISON.

LUÍS TEODORO¹, ENZO BRANCHINI² AND CARLOS S. FRENK³¹T-8, Theoretical Division, Los Alamos National Laboratory, Los Alamos, New Mexico, 87545, USA²Dipartimento di Fisica, Università degli Studi Roma TRE, Roma, Italia³Department of Physics, University of Durham, Science Laboratories, Durham DH1 3LE, England.*Draft version November 12, 2018*

ABSTRACT

We have used the two *IRAS* redshift surveys, 1.2-Jy (Fisher *et al.* 1995) and *PSCz* (Saunders *et al.* 2000), to model the linear velocity fields within a redshift of 8000 km s⁻¹ and have compared them in redshift space. The two velocity fields only differ significantly in their monopole components. The monopole discrepancy cannot be solely ascribed to shot-noise errors and incomplete sky coverage. The mismatch seems to arise from incompleteness of the *PSCz* catalog at fluxes ≤ 1.2 Jy. The 1.2-Jy and *PSCz* higher order velocity multipoles, particularly the dipole and quadrupole components, appear to be consistent, suggesting that the dipole residuals found by Davis, Nusser and Willick (1996) when comparing 1.2-Jy and *Mark III* velocity fields probably originates from the *Mark III* velocities calibration procedure rather than from uncertainties in the model velocity field. Our results illustrate the efficiency of the spherical harmonics decomposition techniques in detecting possible differences between real and model velocity fields. Similar analyses shall prove to be very useful in the future to test the reliability of next generation model velocity fields derived from new redshift catalogs like 2dFGRS (Colless *et al.* 2001), SDSS (York *et al.* 2000), 6dF and 2MRS.

Subject headings: cosmology — theory — galaxies large-scale structure of the Universe — large-scale dynamics.

1. INTRODUCTION

In the framework of linear gravitational instability theory and linear biasing a comparison between the predicted and observed peculiar velocities allows us to measure the so called β parameter

$$\beta \equiv \frac{\Omega_m^{0.6}}{b}. \quad (1)$$

i.e. a combination of the mass density parameter, Ω_m , and the linear bias parameter, b , which relates the mass overdensity field δ to the density fluctuations in galaxy counts δ_g , through $\delta_g = b\delta$. Several different techniques have been used to compare measured peculiar velocities (taken from all available catalogs: *Mark III* Willick 1997a, SFI Haynes 1999, ENEAR da Costa *et al.* 2000, SEcat Zaroubi 2002) to predict velocities that, in most cases, have been obtained from two redshift surveys of *IRAS* galaxies: the 1.2-Jy and the *PSCz* catalogs.

Most analyses have investigated the consistency between model and observed velocities, while only a few of them have been devoted in comparing different datasets or in studying the consistency of model velocity fields. All recent works show a general consistency between models and data (Willick *et al.* 1997, hereafter WSDK; Willick and Strauss 1998; Sigad *et al.* 1998; Dekel *et al.* 1999; Branchini *et al.* 1999, hereafter B99; Nusser *et al.* 2000; Zaroubi *et al.* 2002) with one noticeable exception represented by the work of Davis, Nusser & Willick (1996, hereafter DNW). Their analysis showed that the velocity residuals between the *Mark III* peculiar velocities and the 1.2-Jy predictions display a significant spatial correlation. Subsequent analyses by WSDK and Willick and

Strauss (1998) were performed using the same dataset, a similar model velocity field but a different comparison technique, called VELMOD, which allows for independent calibrations of *Mark III* velocities in each of the *Mark III* sub-catalogs. As a result the observed and model velocity fields were brought into better agreement, at least within a redshift distance $s = 7500$ km s⁻¹ and returned a calibration inconsistent with the original one performed by Willick *et al.* (1997a).

While these results suggest that the DNW mismatch originates from calibration problems in the *Mark III* catalog, the possibility that systematic errors in the 1.2-Jy model velocities also contribute to the discrepancy has been completely overlooked. In particular, we ignored whether the velocity fields predicted from the deeper *IRAS PSCz* catalog provides a better match to the *Mark III* velocities than the shallower 1.2-Jy catalog, considered by DNW.

The main goal of this work is to check whether the discrepancies between the 1.2-Jy and *Mark III* velocities can be ascribed, at least to some extent, to model uncertainties. For this purpose we compare both the overdensity and the radial velocity fields modeled from the redshift space distribution of 1.2-Jy and *PSCz* galaxies. This work is meant to stress the usefulness of spherical harmonics decomposition techniques in assessing the adequacy of a model velocity (or density) field through velocity-velocity (or density-density) comparisons.

In § 2 we describe how to compare velocity and overdensity fields inferred from different redshift surveys. The galaxy redshift catalogs used in our analyses are described in § 3. In sections 4 and 5 we analyse the two model overdensity fields and radial velocity fields. Our main results are discussed in § 6

and our main conclusions are presented in § 7.

2. SPHERICAL HARMONIC COEFFICIENTS DECOMPOSITION

The relations between an arbitrary scalar field $\psi(\mathbf{s})$ and the real-valued spherical harmonic coefficients $\psi_{lm}(s)$ are

$$\psi_{lm}(s) = \int \psi(\mathbf{s}) \mathcal{Y}_{lm}(\hat{\mathbf{s}}) d\Omega \quad (2)$$

$$\psi(\mathbf{s}) = \sum_{l=0}^{\infty} \sum_{m=-l}^l \psi_{lm}(s) \mathcal{Y}_{lm}(\hat{\mathbf{s}}), \quad (3)$$

where $\mathcal{Y}_{lm}(\hat{\mathbf{s}}) \{l = 0, \dots, \infty; |m| \leq l\}$ denote the well known real-valued spherical harmonics, defined as in Baker *et al.* (1999, hereafter BDSLS) and Bunn (1995) (see also Jackson 1999). For a given l these functions are normalized to the value of \mathcal{Y}_{l0} at the North Galactic Pole.

The amplitude of the l -multipole $\psi_l(s)$ is defined by the sum in quadrature over the $(2l+1)$ - ψ_{lm} 's, where $\{m = -l, \dots, l\}$:

$$\psi_l(s) = \left[\sum_{m=-l}^{m=l} \psi_{lm}^2(s) \right]^{\frac{1}{2}}. \quad (4)$$

2.1. Peculiar velocity and overdensity fields from the distribution of galaxies in redshift space

Nusser & Davis (1994) show that in the linear regime the peculiar velocity field is irrotational not only in real space but also in redshift space and thus can be expressed as the gradient of a scalar velocity potential: $\mathbf{v}(\mathbf{s}) = -\nabla\Phi(\mathbf{s})$. At a given redshift s , $\Phi(s)$ and $\hat{\delta}(s)$ can be expanded in spherical harmonics and related to each other through a modified Poisson equation:

$$\frac{1}{s^2} (s^2 \Phi'_{lm})' - \frac{1}{1+\beta} \frac{l(l+1)\Phi_{lm}}{s^2} = \frac{\beta}{1+\beta} \left(\hat{\delta}_{lm} - \frac{1}{s} \frac{d \ln \phi}{d \ln s} \Phi_{lm}' \right), \quad (5)$$

where $\phi(s)$ and $\hat{\delta}_{lm}(s)$ denote the sample selection function and the spherical components of the overdensity field, respectively. Here prime expresses d/ds . Solving this differential equation requires computing the redshift space density field from the observed galaxy distribution on a spherical grid using Gaussian cells of approximately equal solid angle. These cells are equally distributed in longitude (64 bins) and are centered at the Gaussian-Legendre 32 point quadrature formula in the range $-1 \leq \cos(b) \leq 1$, where b is the Galactic latitude. In this work we measure redshifts in the Local Group frame, and use 52 Gaussian radial redshift bins out to a distance of $s = 18000 \text{ km s}^{-1}$. When comparing two or more galaxy catalogs the size of the radial bin is set by requiring equal spatial resolution and the minimal shot noise constant throughout the volume. We do this setting the distance between the centers of the Gaussian cells at distance s equal to the average galaxy-galaxy separation, $\sigma(s) = [\bar{n}\phi(s)]^{-1/3}$, in the sparser catalog. The mean number density is estimated as

$$\bar{n} = \frac{1}{V} \sum_i \frac{1}{\phi(s_i)}, \quad (6)$$

where the sum is over the galaxies contained within the volume V , which, in this work, is a sphere of radius 8000 km s^{-1} .

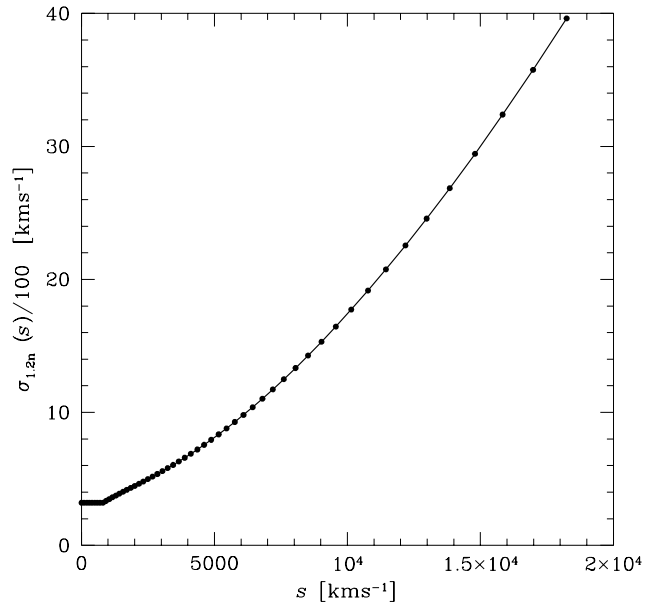


FIG. 1.— The 1.2-Jy smoothing width as a function of redshift. The dots represent the value of σ_n at centre of the 52 redshift bins.

Hernquist and Katz (1989) pointed out that there are two possible ways to estimate the smoothed density field: the "scatter" and "gather" approaches. In the former approach each particle is distributed in space, and the density estimate at a given point is the superposition of individual smoothing spheres. In the latter case one defines a smoothing length at a given point and weights the particle in its neighborhood by the resulting kernel. The Gaussian-smoothed galaxy overdensity field at a grid cell centred around \mathbf{s}_n is given by:

$$1 + \hat{\delta}(\mathbf{s}_n) = \frac{1}{(2\pi)^{3/2} \sigma_n^3} \sum_i^N \frac{1}{\phi(s_i)} \exp \left[-\frac{(\mathbf{s}_n - \mathbf{s}_i)^2}{2\sigma_n^2} \right], \quad (7)$$

where the sum is over the N galaxies in the catalog, which clearly is a "gather" approach. The smoothing width at a redshift s , used in this paper is $\sigma_n = \max[320, \sigma(s)] \text{ km s}^{-1}$. Since in this work we compare the PSCz catalog with the sparser 1.2-Jy catalog, we use the σ_n obtained from the 1.2-Jy catalog shown in Fig. (1). This smoothing scheme is tailored to keep the shot-noise uncertainty roughly constant throughout the sample volume and is similar to the optimal Wiener filtering procedure used by Lahav *et al.* (1994) and Fisher *et al.* (1995b). Moreover, the our kernel has a compact support, which simplifies the computational task.

Eqn. (5) is valid in the linear regime, where a one-to-one mapping between distance and redshift is guaranteed. This assumption is not valid in high density regions, such as cluster of galaxies, where shell crossing may occur triple valued-regions may appear. To deal with the latter effect, we adopt the same procedure as Yahil *et al.* (1991) and collapse the fingers of God associated with the six richest clusters in the sample listed in Table 2 of that work.

In this work we will consider galaxies within $s_{\max} = 20000$

km s^{-1} with the spherical harmonics decomposition limited to $l_{\text{max}} = 15$. Outlying s_{max} galaxies are assumed to be distributed uniformly according to the mean number density of the parent catalogs.

3. DATASETS

The *IRAS PSC_z* catalog contains $\approx 15\,500$ *IRAS PSC* galaxies with a $60\ \mu\text{m}$ flux larger than $0.6\ \text{Jy}$. The average depth of this survey is $\approx 100\ h^{-1}\ \text{Mpc}$. We restrict our analysis to a sub-sample of $11\,206$ galaxies within $20\,000\ \text{km s}^{-1}$ from the Local Group (LG, hereafter). The areas not covered by the survey amount to 16.0% of the sky and are preferentially located near the galactic plane, in the so-called Zone of Avoidance (Saunders *et al.* 2000). The empty areas have been filled-in with the cloning procedure described in Branchini *et al.* (1999).

The 1.2-Jy catalog (Fisher *et al.* 1995a) contains $5\,331$ *IRAS* galaxies with a $60\ \mu\text{m}$ flux larger than 1.2-Jy within $20\,000\ \text{km s}^{-1}$. This catalog has a slightly larger sky coverage of ($\approx 87.6\%$) and a smaller median redshift ($\approx 84\ h^{-1}\ \text{Mpc}$). The same B99 filling technique has been used to restore all sky coverage.

Fisher *et al.* (1995b) have found that uncertainties in filling-in the empty areas of the 1.2-Jy survey do not appreciably affect the spherical harmonics coefficients with $l \lesssim 15$. Similar conclusions are also valid for the *IRAS PSC_z* survey (Teodoro *et al.* 1999).

The selection functions of the two surveys, that quantify the probability of a galaxy at distance s , have been determined as maximum-likelihood fits to the smooth function

$$\phi(s) = \begin{cases} \left(\frac{r}{r_s}\right)^{2\alpha} \left(\frac{r^2 + r_s^2}{r_s^2 + r^2}\right)^\beta & , s \geq H_0 r_s, \\ 1 & , \text{otherwise}, \end{cases} \quad (8)$$

where $r = s/H_0$ ¹ is expressed in $h^{-1}\ \text{Mpc}$ (Yahil *et al.* 1991). The best-fit parameters, determined using the galaxies within $8\,000\ \text{km s}^{-1}$ and assuming a flat universe with $\Omega_m = 1$, are shown in Tab. (1). The quantity r_s in Eqn. (8) accounts for the incompleteness of faint galaxies in the innermost regions of the catalogs (Rowan-Robinson *et al.* 1990, Yahil *et al.* 1991).

4. THE *IRAS PSC_z* AND 1.2-Jy FIELDS OVERDENSITY

The first step of our analysis consists of applying Eqn. (7) to compute the *IRAS* 1.2-Jy and *PSC_z* overdensities onto a spherical grid of radius $18\,000\ \text{km s}^{-1}$ and $l_{\text{max}} = 15$ with the smoothing scheme given by Eqn. (7).

4.1. Overdensity Maps

In Figs. (2–4) we show the Aitoff projections of the *PSC_z* (top panels) and 1.2-Jy (middle panels) galaxy overdensity fields in three spherical shells centred at $s = 1\,000, 3\,000$ and $5\,000\ \text{km s}^{-1}$, respectively. The thickness of each shell is defined by the Gaussian width at the distance of the shell. All maps are plotted in Galactic coordinates. The bottom panels show the map of the

¹Throughout this article we write Hubble's constant as $H_0 = 100h\ \text{km s}^{-1}\ \text{Mpc}^{-1}$

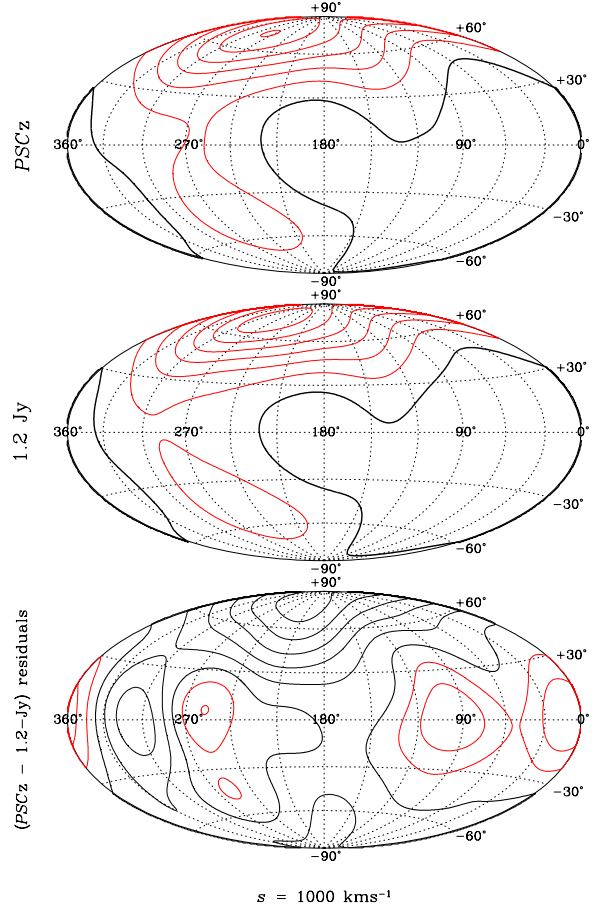


FIG. 2.— *PSC_z* (top), 1.2-Jy (middle) and residual (bottom) overdensity fields in the radial shell centred at $s = 1000\ \text{km s}^{-1}$. The thick-line contour indicates $\delta = 0$ or $\delta_{\text{res}} = 0$ (bottom). The light- and dark-gray contours show over- and under-dense regions, respectively. In the top and middle panels the contours are equally-spaced by $\Delta\delta = 1.0$. The bottom panel the density residuals are shown in steps of $\Delta\delta_{\text{res}} = 0.125$.

overdensity residuals $\delta_{\text{res}}(s) = \delta_{0.6}(s) - \delta_{1.2}(s)$, where the subscripts _{0.6} and _{1.2} refer to *PSC_z* and 1.2-Jy surveys, respectively. In all plots the thick line indicates the zero overdensity (or residual) contour. The overdensity (residual) contour spacing $\Delta\delta$ ($\Delta\delta_{\text{res}}$) depends on the shell's depth and is indicated in the Figure captions. Detailed cosmographic studies of the structures in the nearby universe have already been performed using both the distribution of 1.2-Jy (Strauss and Willick 1995) and *PSC_z* galaxies² and will not be repeated here. We only stress that the main cosmic structures like the Virgo Cluster ($l \approx 240^\circ, b \approx 75^\circ, s = 1000\ \text{km s}^{-1}$), the local void spanning the region $330^\circ \lesssim l \lesssim 120^\circ, -90^\circ \lesssim b \lesssim 30^\circ$ at $s = 1000\ \text{km s}^{-1}$, the Hydra-Centaurus complex ($l \approx 270^\circ, b \approx 20^\circ, s = 3000\ \text{km s}^{-1}$) and ($l \approx 300^\circ, b \approx 20^\circ, s = 3000\ \text{km s}^{-1}$) and the Perseus-Pisces supercluster ($l \approx 140^\circ, b \approx -25^\circ, s = 3000\ \text{km s}^{-1}$) are detected in both surveys.

The residuals, calculated at the same gridpoints as the den-

²See <http://www-astro.physics.ox.ac.uk/~wjs/psc2.html>

TABLE 1
SELECTION FUNCTION PARAMETERS FOR *IRAS* CATALOGS.

Catalog	$f_{60\mu m}^{\lim}$ [Jy]	N_{gal}^a	α	β	γ	r_s^b [h^{-1} Mpc]	r_* [h^{-1} Mpc]	\bar{n} [h^3 Mpc $^{-3}$]
<i>PSC_z</i>	0.6	13 364	0.54	1.80	...	6.0	87.00	$6.12 \cdot 10^{-2}$
<i>PSC_z 0.7</i>	0.7	11 170	0.57	1.80	...	6.0	76.35	$6.38 \cdot 10^{-2}$
<i>PSC_z 1.2</i>	1.2	5 519	0.43	1.86	...	5.0	50.40	$4.62 \cdot 10^{-2}$
1.2-Jy	1.2	6 010	0.43	1.86	...	5.0	50.60	$4.67 \cdot 10^{-2}$
<i>PSC_z^c</i>	0.6	13 364	0.99	3.45	1.93	6.0	76.02	$5.76 \cdot 10^{-2}$

^a Includes synthetic objects.

^b Parameter kept constant in the likelihood maximization.

^c The selection function parameters have been taken from Canavezes *et al.* (1999)

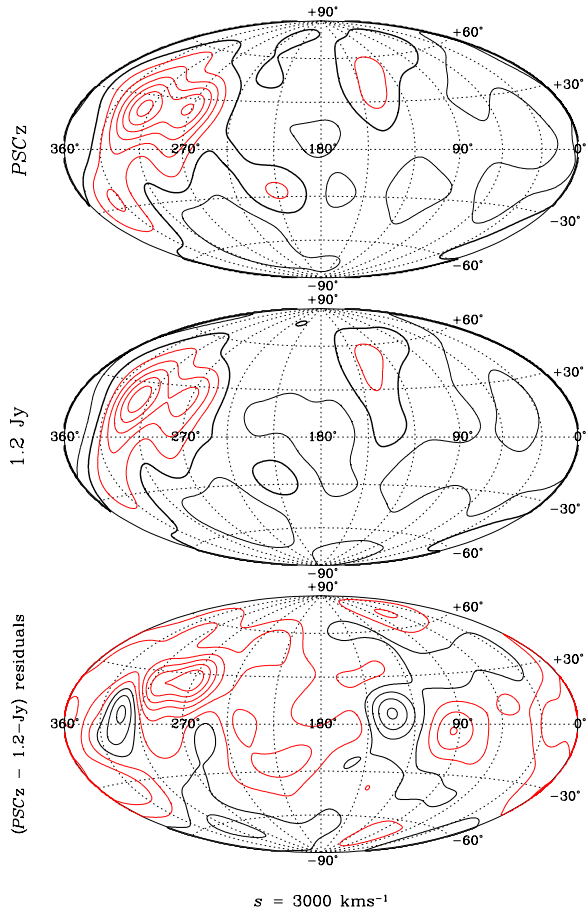


FIG. 3.— Same as in Fig. (2). The shell is now centred at $s = 3000$ km s $^{-1}$ and the contour spacings are $\Delta\delta = 0.5$ and $\Delta\delta_{\text{res}} = 0.125$.

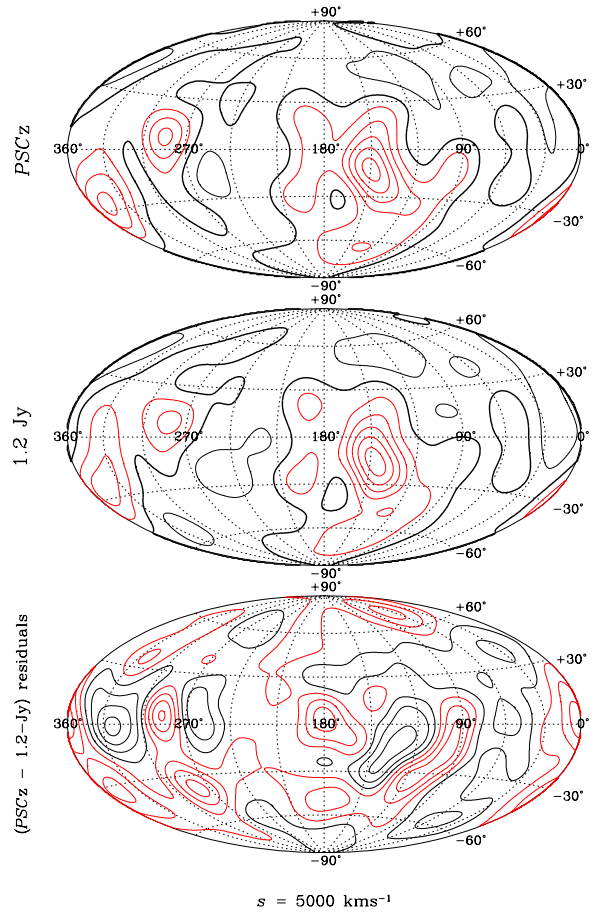


FIG. 4.— Same as in Fig. (2). The shell is now centred at $s = 5000$ km s $^{-1}$ and the contour spacings are $\Delta\delta = 0.5$ and $\Delta\delta_{\text{res}} = 0.125$.

TABLE 2
THE PARAMETERS OF THE $\delta_{1.2} - \delta_{0.6}$ AND $u_{1.2} - u_{0.6}$ LINEAR REGRESSIONS.

Regression	N_{grid}	N_{dof}	A^a	B	$\chi^2_{\text{eff}}/N_{\text{dof}}$
$\delta_{1.2} - \delta_{0.6}$	112 552	156.36	-0.011 ± 0.014	1.025 ± 0.036	0.78
$u_{1.2} - u_{0.6}$	112 552	$\lesssim 156.36$	60.0 ± 5.9	1.040 ± 0.019	0.88

Notes:

^a For the $u - u$ comparison A is expressed in km s^{-1} .

Column 2: N_{grid} , the number of gridpoints used for the regression;

column 3: N_{dof} , the number of independent volumes;

column 4: A , the zero-point offset in the linear regression, and its $1 - \sigma$ error;

column 5: B , the slope of the linear regression, and its $1 - \sigma$ error;

column 6: $\chi^2_{\text{eff}}/N_{\text{dof}}$ from the linear regression.

sity fields, seem to indicate that, as expected, the largest residuals are located near the galactic plane where uncertainties in the filling-in procedure dominate the errors. In the inner shell, overdensities in the 1.2-Jy galaxy distribution appear to be larger than the *PSCz* ones while in the most external shell the situation is reversed.

4.2. Density Residuals

A way of quantifying possible systematic differences between the two fields is that of performing a point-to-point comparison. In absence of systematic errors we expect the two IRAS overdensity fields to be linearly related through

$$\delta_{1.2} = B\delta_{0.6} + A \quad (9)$$

with $A = 0$ and $B = 1$. $\delta_{0.6}$ and $\delta_{1.2}$ are estimated at Cartesian gridpoint positions. A zero-point offset $A \neq 0$ indicates discrepancies in the mean densities of the two catalogs while a slope $B \neq 1$ reveals the presence of systematic errors. If the values of $\delta_{0.6}$ and $\delta_{1.2}$ are independent and their errors are Gaussian then we can compute the χ^2 statistics

$$\chi^2 = \sum_{i=1}^{N_{\text{grid}}} \frac{(\delta_{1.2} - A - B\delta_{0.6})^2}{(\sigma_{1.2}^2 + B^2\sigma_{0.6}^2)}, \quad (10)$$

where $\sigma_{0.6}$ and $\sigma_{1.2}$ indicate the typical errors in δ and N_{grid} is the total number of points in the comparison. However, since the gridspacing (250 km s^{-1}) is smaller than the smoothing length ($\geq 320 \text{ km s}^{-1}$), not all values of $\delta_{0.6}$ (or $\delta_{1.2}$) are independent. Indeed, the effective number of independent points used in the χ^2 statistics, N_{eff} is given by

$$N_{\text{eff}}^{-1} = N_{\text{grid}}^{-2} \sum_{i=1}^{N_{\text{grid}}} \sum_{j=1}^{N_{\text{grid}}} \exp(-r_{ij}^2/2R_{s,i}^2), \quad (11)$$

where r_{ij} is the separation between gridpoints i and j and $R_{s,i}$ is the smoothing radius of the Gaussian kernel at the gridpoint

i. This expression is a generalization of Eqn. (12) in Dekel *et al.* (1993) to the case of a grid with variable mesh-size since $R_{s,i}$ depends on the gridpoint position. The new statistics $\chi^2_{\text{eff}} = (N_{\text{grid}}/N_{\text{eff}})\chi^2$ is approximately distributed as a χ^2 with $N_{\text{dof}} = N_{\text{eff}} - 1$ degrees of freedom and can be applied to infer the values of A , B and their errors.

Fig. (5) shows the $\delta_{1.2}$ vs. $\delta_{0.6}$ scatter diagram obtained using all 112 552 gridpoints with $s < 8000 \text{ km s}^{-1}$ and $|b| > 8^\circ$. Within these limits the estimated overdensities are little affected by uncertainties in the filling-in procedure, and we expect that

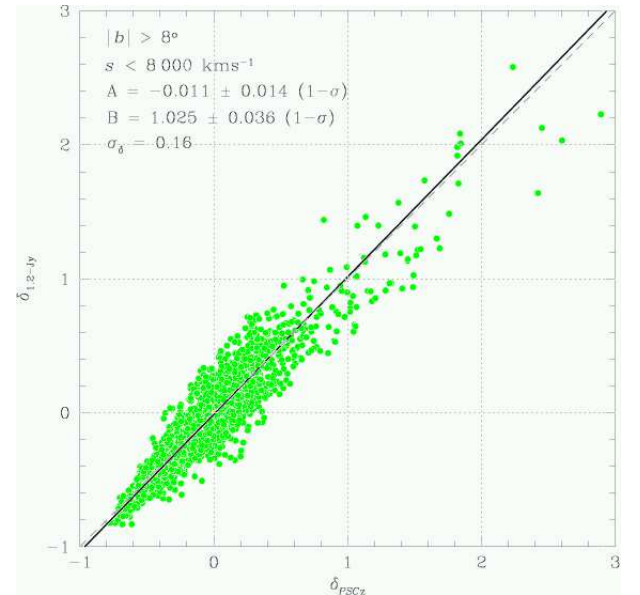


FIG. 5.— 1.2-Jy vs. *PSCz* overdensity. Only 1883 randomly selected gridpoints with $|b| > 8^\circ$ and within $s = 8000 \text{ km s}^{-1}$ are shown in the scatter plot. The continuous line represents the linear best fit characterized by the zeropoint A and slope B indicated in the panel.

shot-noise dominates the total error budget. To estimate the shot-noise errors affecting both *PSCz* and 1.2-Jy overdensity fields we have generated 100 bootstrap realizations of the observed *PSCz* and 1.2-Jy surveys. These are obtained by replacing each galaxy (including the ‘synthetic’ galaxies used to fill-in the unobserved regions) with a number of objects drawn from a Poisson deviate with mean unity. Shot noise errors in δ at the generic gridpoint were set equal to the dispersion over the 100 realizations. The solid line in the plot is the best linear fit obtained from the minimization of χ^2_{eff} . As shown in Tab. (2), the slope of the line, $B = 1.025 \pm 0.036$, is consistent with unity, indicating no systematic mismatch. On the other hand the zero-point value $A = -0.011 \pm 0.014$ shows no systematic difference in the mean density of the two *IRAS* catalogs.

The scatter around the best-fitting line, $\sigma_\delta = 0.16$ is similar to average shot-noise error in the 1.2-Jy density field ($\sigma_{\delta_{\text{SN}}}^{\delta_{1.2}} = 0.15$). The parameter $S = \chi^{\text{eff}}/N_{\text{dof}} = 0.78$ indicates that bootstrap errors slightly overestimate the true uncertainties.

4.3. Radial Density Contrast

An alternative way to characterize possible discrepancies between the two *IRAS* density fields is that of computing the differential radial density contrast in shells with identical thickness Δs for both galaxy distributions:

$$\frac{\rho(s)}{\bar{\rho}} = \frac{1}{V\bar{n}} \sum_{i=1}^{N_p} \frac{W(s, s_i, \Delta s)}{\phi(s_i)}, \quad (12)$$

where the window associated to the spherical shell $W_{\delta\rho/\bar{\rho}}(s, s_i, \Delta s)$ is the Heaviside function $H(s + \Delta s/2 - s_i)H(s_i + \Delta s/2 - s)$, s_i is the redshift of the object i , V is the volume used to compute the mean number density \bar{n} and the sum runs over the N_p galaxies of the catalog. Fig. (6) shows the quantity $\rho(s)/\bar{\rho}$ for 1.2-Jy (light, dotted histogram) and *PSCz* (thick, continuous histogram) galaxies within $s = 15000 \text{ km s}^{-1}$, computed in spherical shells of thickness $\Delta s = 200 \text{ km s}^{-1}$. Although the general shapes of two radial density contrasts are similar (with a bump at $s \sim 1100 \text{ km s}^{-1}$ due to Virgo and Fornax clusters, a dip at $s \sim 3500 \text{ km s}^{-1}$ induced by the Sculptor Void and a second prominent peak at $s \sim 5000 \text{ km s}^{-1}$, at the same redshift as the Perseus-Pisces supercluster and the Great Attractor), a discrepancy between the two curves exists in the range $2000 \lesssim s \lesssim 6000 \text{ km s}^{-1}$ where the *PSCz* density is larger than the 1.2-Jy one.

The two smoothed curves in Fig. (6) show the monopole terms of the two overdensity fields $\delta_{l=0, m=0}$ as a function of radius, obtained from the spherical harmonics decomposition. Both curves interpolate the histograms rather well (hence showing the adequacy of our spherical harmonics analysis) and confirm the existence of a *PSCz* vs. 1.2-Jy density mismatch between the two catalogs.

5. THE *IRAS* *PSCz* AND 1.2-Jy PECULIAR VELOCITY FIELDS

To perform a similar analysis on the 1.2-Jy and *PSCz* model velocity fields we have integrated Eqn. (5) using $\beta = 0.6$, a value

consistent with recent determinations based on several velocity-velocity comparisons (e.g. Nusser *et al.* 2000), a recent density-density analysis (Zaroubi *et al.* 2002) and the study of mean relative velocities of galaxy pairs (Juszkiewicz *et al.* 2000).

5.1. Radial Peculiar Velocity Maps

To obtain maps of the radial velocity field we have computed the gradient of the velocity potential projected along the line of sight: $u(\mathbf{s}) = \hat{\mathbf{s}} \cdot \nabla \Phi$ at the same gridpoint positions used for the analysis of the density field.

The top end mid panels of Figs. (7-9) are similar to those of figs. 2-4 and show the radial velocity maps in the same shells. The bottom panels show the maps of the radial velocity residuals $u_{\text{res}}(s) \equiv u_{0.6}(s) - u_{1.2}(s)$. The thick line represents the zero radial velocity (residual) contour. The velocity (residual) contour spacing Δu (Δu_{res}) varies with the redshift and is indicated in the Figure captions.

The main feature seen at all redshifts in both 1.2-Jy and *PSCz* radial velocity maps is the dipole pattern resulting from the LG reflex motion toward the CMB apex ($l \approx 276^\circ, b \approx 30^\circ$, Kogut *et al.* 1993).

Local deviations from this pattern arise from peculiar motions, like the infall onto Perseus-Pisces superclusters at ($s \approx 3000 \text{ km s}^{-1}, l \approx 120^\circ, b \approx -40^\circ$). The largest velocity residuals are located near the galactic plane, but their contours are broader due to the intrinsic non-locality of the peculiar velocity field. The most striking feature is perhaps the fact that velocity residuals, that are positive across a large fraction of the sky in the first shell, becomes mostly negative in the remaining two shells, suggesting possible systematic errors in either *PSCz* or 1.2-Jy velocity models.

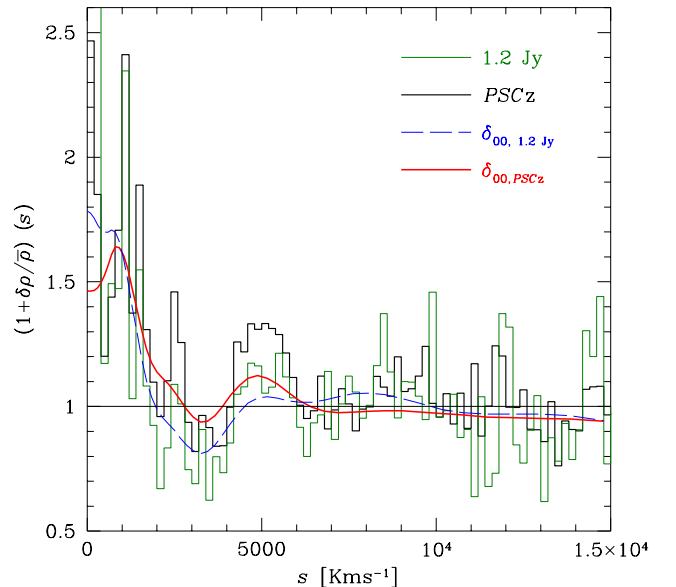


FIG. 6.— Differential radial density contrast for *PSCz* (thick line histogram) and 1.2-Jy galaxies (thin line histogram). The monopole of the *PSCz* and 1.2-Jy density fields are shown with smooth solid and dashed lines, respectively.

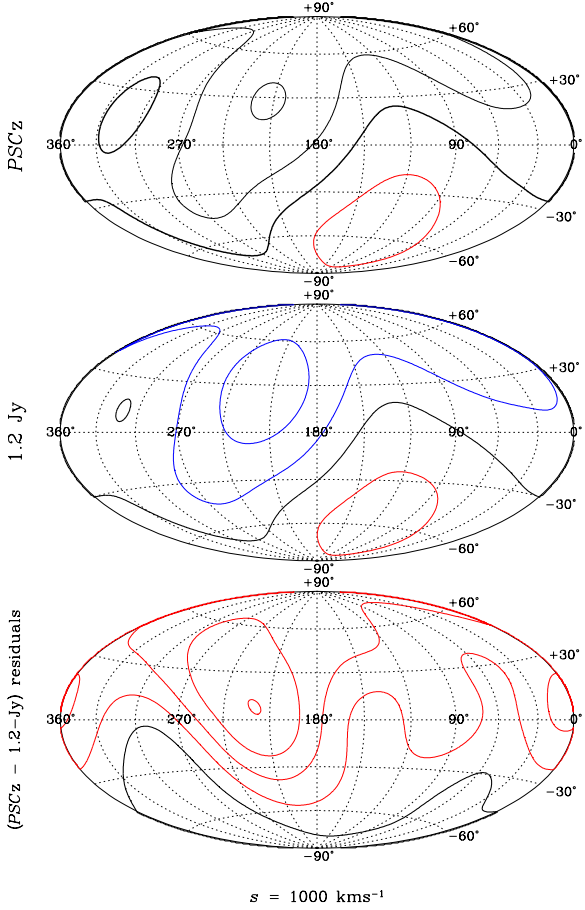


FIG. 7.— PSC_z (top), 1.2-Jy (middle) and residual (bottom) radial velocity fields in the spherical shell centred at $s = 1000 \text{ km s}^{-1}$. The thick-line contour indicates $\delta u = 0$ or $\Delta u_{\text{res}} = 0$. The light- and dark-gray contours show regions characterized by outflows or infall motions. In the top and middle panels the contours are equally-spaced by $\Delta u = 200 \text{ km s}^{-1}$. The bottom panel shows the velocity residuals in steps of $\Delta \delta_{\text{res}} = 25 \text{ km s}^{-1}$.

5.2. Velocity Residuals

To perform a more quantitative comparison between the two radial velocity fields we have repeated the analysis of § 4.2 and performed a linear regression between $u_{1.2}$ and $u_{0.6}$ by minimizing

$$\chi^2 = \sum_{i=1}^{N_{\text{grid}}} \frac{(u_{1.2} - A - B\sigma_{u,0.6})^2}{(u_{1.2}^2 + B^2\sigma_{u,0.6}^2)}, \quad (13)$$

where N_{grid} runs over the same points used for the density-density comparison. Linear velocities are obtained by integrating the mass density fields over large scales causing them to be correlated on scales larger than the radius of the Gaussian kernel. This means that the number of independent gridpoint N_{eff} is smaller than the estimate given by Eqn. (11). Intrinsic large scale smoothing also affects the velocity error estimate, σ_u since uncertainties in modeling the galaxy distribution in the unobserved areas now add to shot noise errors.

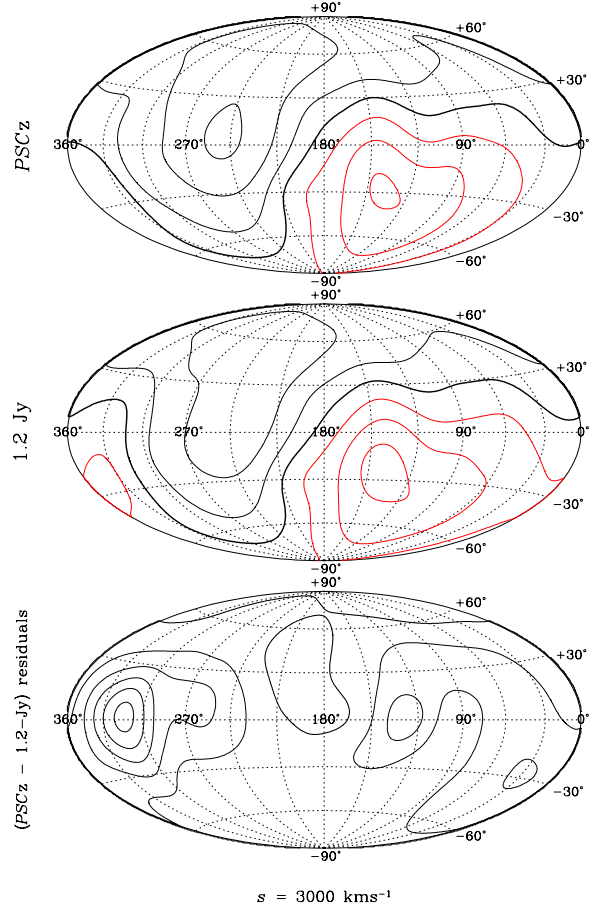


FIG. 8.— Same as in Fig. (7). The shell is now centred at $s = 3000 \text{ km s}^{-1}$ and the contour spacings are $\Delta u = 200 \text{ km s}^{-1}$ and $\Delta u_{\text{res}} = 50 \text{ km s}^{-1}$

The shot noise errors have been computed using the same bootstrap resampling technique described in § 4.2. Uncertainties in the filling-in procedure have been evaluated from 20 independent PSC_z and 1.2-Jy mock catalogs extracted from the N -body simulations performed by Cole *et al.* (1997) simulating a volume of $\approx 170 h^{-1} \text{ Mpc}$ in an Einstein-de Sitter universe with a non-vanishing ($\Omega_\Lambda = 0.7$) cosmological constant and density fluctuations normalized to the observed cluster abundance (Eke, Cole & Frenk 1996). Model velocity fields from each IRAS mock catalog were compared with velocities obtained from ideal, all-sky IRAS mock catalogs. The variance over 20 mocks at each gridpoint quantifies the uncertainties in the filling procedure. Total uncertainties were obtained by adding in quadrature the two errors.

The results of the linear regression are summarized in Tab. (2) which shows the slope of the best fitting line $B = 1.040 \pm 0.019$ and the value of the zero-point, $A = 60.0 \pm 5.9 \text{ km s}^{-1}$. While the slope is still consistent with unity, at the 2.1σ confidence level, the zero point is significantly different from zero, hence corroborating the evidence for a mismatch in the average densities of PSC_z and 1.2-Jy catalogs. The dispersion around the fit

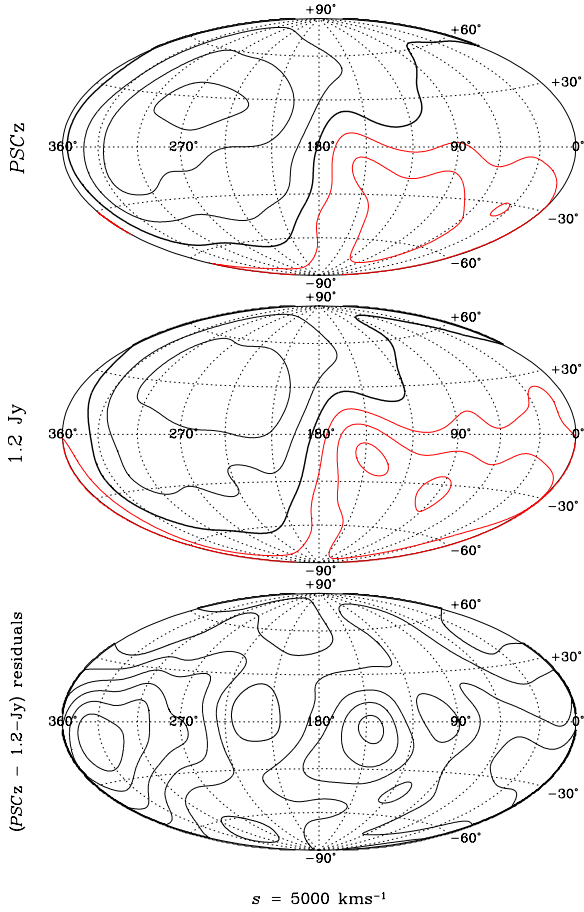


FIG. 9.— Same as in Fig. (7). The shell is now centred at $s = 5000 \text{ km s}^{-1}$ and the contour spacings are $\Delta u = 200 \text{ km s}^{-1}$ and $\Delta u_{\text{res}} = 50 \text{ km s}^{-1}$.

is, $\sigma_u = 88 \text{ km s}^{-1}$ is similar to the typical velocity error computed from the IRAS mocks and the bootstrap resampling catalogs ($\sigma_{u_{0.5}} = 71 \text{ km s}^{-1}$ and $\sigma_{u_{1.2}} = 140 \text{ km s}^{-1}$). The parameter $\chi^{\text{eff}}/N_{\text{dof}}$ is less than unity which either indicates that errors are overestimated or that the value N_{eff} , taken from Eqn. (11), does significantly overestimate the true number of degrees of freedom.

5.3. Velocity Multipoles

The spherical harmonics decomposition allows us to better investigate and characterize possible discrepancies between 1.2-Jy and PSCz velocity fields. Here we are only interested in the first three ($l = 0, 1, 2$) components, corresponding to the monopole, dipole and quadrupole terms, which have already been investigated in previous analyses (e.g. BDSLS). It is worth stressing that the monopole and dipole components at a given redshift are only sensitive to the mass distribution within the corresponding distance and thus can be directly related to the structures within the volume considered, while the quadrupole components are also sensitive to the mass distribution beyond such a distance [see Eqn. (9) in Nusser & Davis 1994].

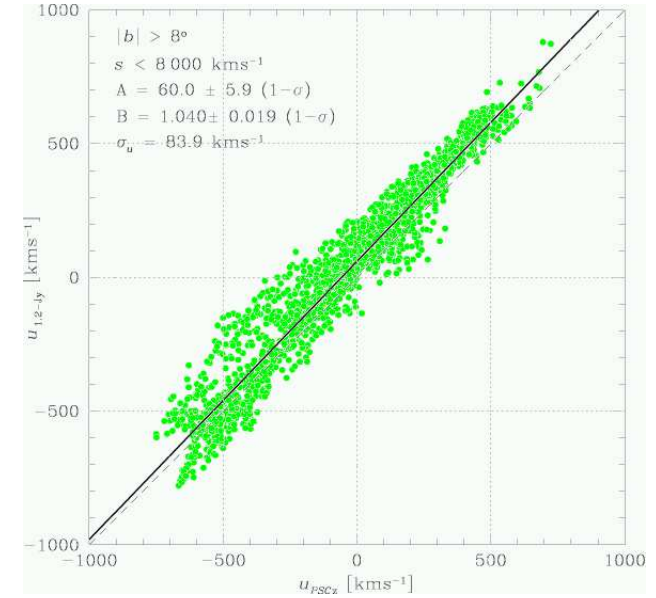


FIG. 10.— 1.2-Jy vs. PSCz radial velocities computed at 1883 randomly selected gridpoint positions with $|b| > 8^\circ$ and $s \leq 8000 \text{ km s}^{-1}$ inferred radial velocity field (x-axis) versus that inferred from the 1.2-Jy survey (y-axis). The parameters of the best fitting line (A, B) the scatter σ_u are indicated.

The monopole terms of PSCz (continuous line) and 1.2-Jy (dashed line) velocity fields are plotted in Fig. (11) as a function of the redshift. The hatched and dashed regions represent the $1-\sigma$ uncertainty strip, computed from the mock catalogs and the bootstrap resampling procedure.

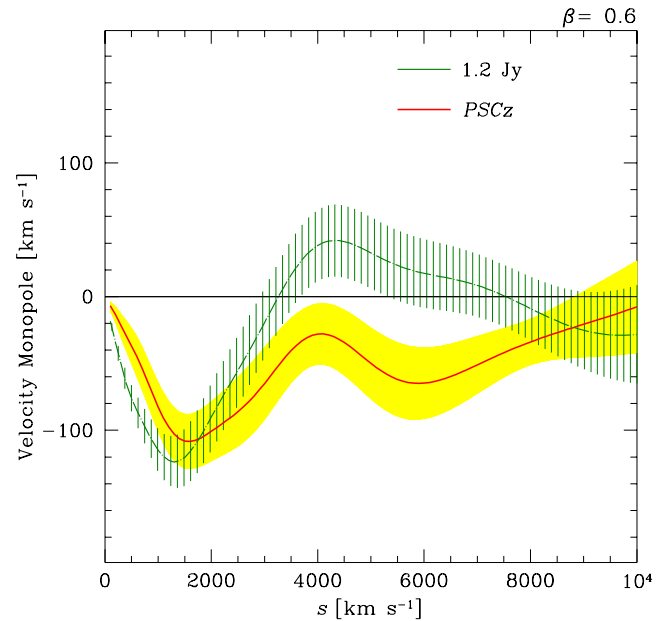


FIG. 11.— Monopole coefficients of 1.2-Jy (dashed) and PSCz (continuous) radial velocity fields. $1-\sigma$ errors are represented by the hatched (shaded) areas.

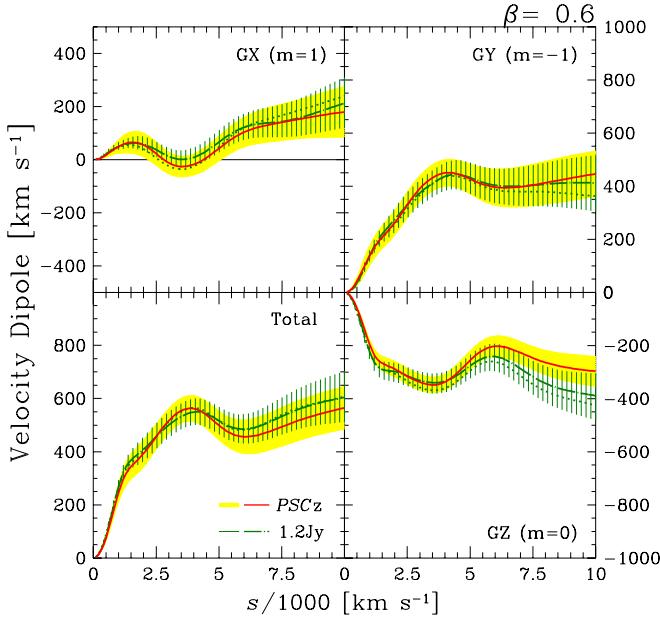


FIG. 12.— The velocity dipole coefficients, $u_{1m}(s)\{m = -1, 0, 1\}$, inferred from $PSCz$ (continuous) and 1.2-Jy (dashed) and their associated $1-\sigma$ uncertainties. The three Galactic Cartesian components GX , GY , GZ are shown in the top-left, top-right and bottom-right panel, respectively. The total amplitude is shown in the bottom-left panel. The dotted line refers to the dipole of $PSCz$ galaxies with flux $f_{60\mu m} \geq 1.2$ Jy.

Both velocity monopoles display the same general features, as expected given the similarities between the density monopoles $\delta_{00}(s)$ shown in Fig. (6). There is a significant radial inflow around $s = 1800 \text{ km s}^{-1}$ corresponding to the infall motion toward the Virgo-Fornax complex, an outflow in the range $1800 \lesssim s \lesssim 4000 \text{ km s}^{-1}$ due to the presence of the local void and another infall beyond this radius, due to the Hercules, Hydra, Centaurus and Perseus-Pisces superclusters. Differences between the two velocity monopoles are detected with a significance level larger than $1-\sigma$ at very small radii ($s < 1200 \text{ km s}^{-1}$) and in the range $3500 \text{ km s}^{-1} < s < 7500 \text{ km s}^{-1}$.

Fig. (12) shows the total amplitude (lower left panel) and the three Cartesian components (remaining panels) of the two IRAS velocity dipoles. The total amplitude of the $PSCz$ dipole (continuous line) is systematically smaller than the 1.2-Jy one (dashed line) but the discrepancy is well within the expected errors, in agreement with previous studies (e.g. Schmoldt *et al.* 1999).

Finally, Fig. (13) shows the five components of the $PSCz$ (continuous line) and 1.2-Jy (dashed line) velocity quadrupoles, $u_{2m}(s)$ (where $m = -2, \dots, 2$) along with total amplitude (bottom-left panel). As for the dipole case, the two sets of quadrupole components agree to within $1-\sigma$ apart from a small disagreement in the $m = +2$ and $m = -2$ components beyond $s = 7000 \text{ km s}^{-1}$. Indeed, beyond $s \approx 6000 \text{ km s}^{-1}$ the amplitude of the $PSCz$ quadrupole decreases, while the 1.2-Jy one increases monotonically.

It is worth noticing that our 1.2-Jy velocity multipoles agree

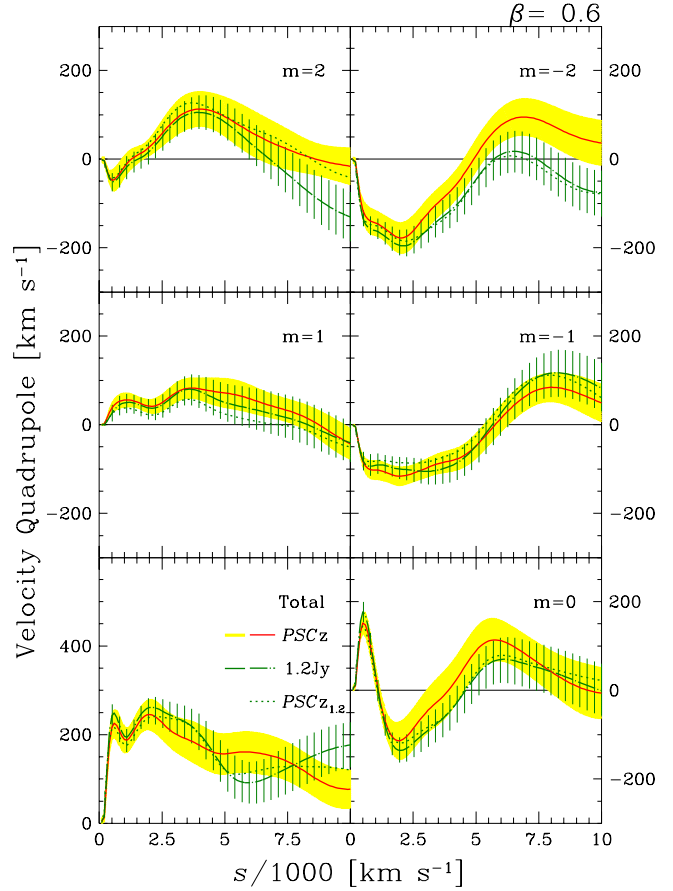


FIG. 13.— Quadrupole coefficients $u_{2m}(s)\{m = -2, \dots, 2\}$ derived from $PSCz$ (solid line) and 1.2-Jy (dashed) model velocity fields. Shaded regions indicate the $1-\sigma$ uncertainty regions. The dotted line represents the quadrupole components for $PSCz$ galaxies with flux $f_{60\mu m} \geq 1.2$ Jy.

with those computed by BDSLS except that their multipole components exhibit sharper features at small radii ($s < 500 \text{ km s}^{-1}$). This mismatch derives from our use of a Gaussian smoothing kernel of radius 330 km s^{-1} which is somewhat larger than that applied by BDSLS.

6. DISCUSSION

Perhaps the most surprising result of our analysis is the disagreement between the $PSCz$ and 1.2-Jy velocity monopoles in the $1800 \lesssim s \lesssim 4000 \text{ km s}^{-1}$ range. Before investigating the possible causes of this mismatch, it is worth noticing that none of our IRAS monopoles is consistent with an outward flow of magnitude $\approx 400 \text{ km s}^{-1}$ at a distance of 7000 km s^{-1} like the one detected by Zehavi *et al.* (1998) using a sample of 44 Type Ia supernovae. That result is also at variance with the velocity model obtained from the distribution of ORS galaxies obtained by BDSLS which means that, if confirmed, it would be difficult to reconcile with the Gravitational Instability scenario.

A possible clue to understand the origin of the monopole mismatch is provided by the analysis of BDSLS that returns a velocity monopole somewhere between the $PSCz$ and 1.2-

Jy ones in the range of interest. This seems to suggest that our monopole discrepancy originates from systematic errors in one of the IRAS catalogs, possibly some incompleteness of the largest catalog at faint fluxes.

The results of Tadros *et al.* (1999) seem to confirm that *PSC_z* catalog might be statistically incomplete at fluxes $f_{60\mu\text{m}} \leq 0.7$ Jy. To test whether this is indeed the case we have extracted a brighter *PSC_z* subsample (called *PSC_{z0.7}*) by discarding all object with $f_{60\mu\text{m}} \leq 0.7$ Jy and have repeated our spherical harmonics decomposition analysis. The results, shown in Fig. (14) indicate that the *PSC_{z0.7}* velocity monopole (dotted line) basically coincide with that of the complete sample. It is only when discarding galaxies with fluxes smaller than 1.2 Jy that the velocity monopole (dashed line) agrees with the 1.2-Jy one.

Another possibility of understanding the monopole mismatch is that of invoking a strong evolution of IRAS galaxies as a function of the redshift, which we have neglected in our calculations so far. Roughly speaking evolution can be distinguish into two different types. Pure density evolution changes only the normalization of the luminosity function while its shape is invariant with redshift. Pure luminosity evolution on the other hand describes a possible change of the intrinsic luminosities of the sources but not their number density. Both forms of evolution occur simultaneously in the Universe. For instance, galaxy merging reduces the number density of galaxies causing thus evolution. Besides, such events also cause different luminosities of the final systems and hence leading to luminosity evolution. Other physical mechanism for galaxy evolution can be devised. Some evidences for a sizable evolution of *IRAS* galaxies have been reported by a number of authors, although there seem to be much controversy about the amplitude of the effect (see Springel 1996 and references therein).

Canavezes *et al.* (1998) expressed evolution in terms of a generalization of the selection function introduced by Yahil *et al.* (1991) given by

$$\phi(s)_{\text{evol}} = \begin{cases} \left(\frac{r_s}{r}\right)^\alpha \left(\frac{r_s^\gamma + r^\gamma}{r_s^\gamma + r^\gamma}\right)^{\beta/\gamma} & , s \geq H_0 r_s, \\ 1 & , \text{otherwise.} \end{cases} \quad (14)$$

Springel (1996) showed that it indeed provides a rather accurate modeling of both *IRAS* data-sets. The estimated parameters using a maximum-likelihood procedure are listed in Tab. (1) and are denoted by *PSC_{zevol}*. The effect of evolution are shown in Fig. (14) in which the velocity monopole term derived from the *PSC_z* galaxy distribution in which evolutionary effects have been accounted for through the new selection function $\phi(s)_{\text{evol}}$ (dot-dashed line) is plotted against the unevolved model. The evolutionary effects are very minor, as was somewhat expected given the locality of our galaxy sample, and do not help in reducing the *PSC_z* vs. 1.2-Jy velocity monopole mismatch.

Overall, our analysis seems to indicate that the discrepancy between 1.2-Jy and *PSC_z* velocity monopoles cannot be ascribed to errors in the modeling of the selection function which, as we have seen, would not change the monopole terms appreciably. Catalog incompleteness at very low fluxes has to be ruled out too. We can only conclude that either the *PSC_z* in-

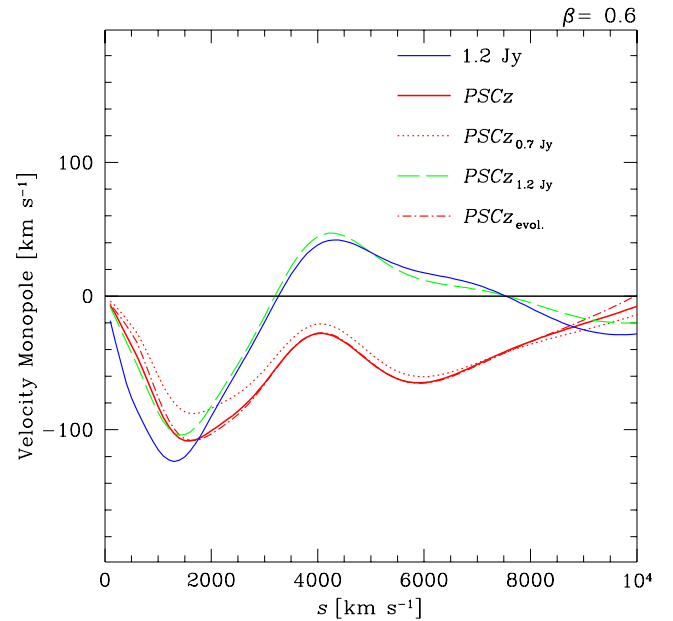


FIG. 14.— Velocity monopoles for the 1.2-Jy (dark gray line) *PSC_z* (light-gray), *PSC_{z0.7}* (dot-dashed), *PSC_{z1.2}* (long-dashed) *PSC_{zevol}* (dotted) samples.

completeness extend at objects with fluxes comparable to 1.2 Jy or that the monopole mismatch does reflect a genuine difference in the average density of faint vs. bright *IRAS* galaxies at $s \leq 4000 \text{ km s}^{-1}$.

A second important result found in our analysis is that the 1.2-Jy and *PSC_z* dipoles agree within the $1-\sigma$ errors. This means that the use of the *PSC_z* rather than the 1.2-Jy catalog does not help in reducing the *Mark III-IRAS* dipole residuals found by Davis, Nusser & Willick (1996). Indeed, both GX and GY components of the *PSC_z* velocity dipole are much too large with respect to *Mark III* ones (see Fig 15 of Davis, Nusser & Willick 1996). Similar results were also obtained from the ORS vs. *Mark III* dipole velocity comparison (BDSLs). We conclude that the discrepancy between the *Mark III* and 1.2-

TABLE 3
SELECTION FUNCTION PARAMETERS IN THE *IRAS* MOCK CATALOGS.

Mock catalog	α	β	r_s [$h^{-1} \text{ Mpc}$]	r_* [$h^{-1} \text{ Mpc}$]
<i>PSC_z</i>	0.53	1.90	10.90	86.40
1.2-Jy	0.48	1.79	5.00	50.40

Jy velocity fields cannot be alleviated by reducing the shot noise errors of the model velocity field.

The agreement between the PSC_z , 1.2-Jy and ORS dipoles is reassuring since it guarantees that uncertainties in model velocity fields arising from within the galaxy samples that derive from incompleteness in one (or more) catalogs, incorrect treatment of non-linear velocities or non-linear non-uniform biasing do not generate systematic errors apart from a the monopole mismatch in the range $1800 \text{ km s}^{-1} \leq s \leq 4000 \text{ km s}^{-1}$.

Unlike the case of monopole and dipole moments, possible differences between the 1.2-Jy and PSC_z quadrupole components can also be attributed to incorrect determination and dilute sampling of the density field beyond the sample. The fact that 1.2-Jy and PSC_z velocity quadrupole agree within the expected errors suggests that differences in the quadrupole components of the two fields can be understood in terms of shot noise errors and uncertainties in filling the empty regions.

With this respect it is worth investigating whether the denser sampling of the PSC_z catalog at large radii allows a better modeling of the large scale contribution to the model velocity field. Indeed, when comparing the model 1.2-Jy velocity field to *Mark III* velocities in the framework of the VELMOD analysis, WSDK have found that velocity residuals exhibit a quadrupole pattern of the form $u_Q = \mathcal{V}_Q \mathbf{r} \cdot \hat{\mathbf{r}}$, where \mathcal{V}_Q is a traceless, symmetric 3×3 tensor. They have attributed this “VELMOD quadrupole” residuals to uncertainties in modeling the IRAS density field beyond 3000 km s^{-1} . In particular they found that the most important sources of uncertainties were the smoothing procedure (based on a Wiener Filtering technique) and the shot noise errors, with the errors deriving from having ignored mass inhomogeneities beyond $12,000 \text{ km s}^{-1}$ playing a minor role. Using PSC_z instead of 1.2-Jy catalog reduces the shot noise errors in the density field beyond 3000 km s^{-1} and thus should improve the agreement with the *Mark III* velocities. In other words one would expect the quadrupole of the residual velocity field $u_{0.6}^> - u_{1.2}^>$, where one only takes in account the mass beyond 3000 km s^{-1} , to be similar to the “VELMOD quadrupole” of WSDK.

In Fig. (15) we compare the VELMOD quadrupole at $s = 2000 \text{ km s}^{-1}$ (rescaled from $\beta = 0.492$ to $\beta = 0.6$, upper panel) to the $u_{0.6}^> - u_{1.2}^>$ quadrupole residual (lower panel). The VELMOD quadrupole reaches its maximum value at ($l \approx 165^\circ$, $b \approx 55^\circ$) and in the opposite direction of the sky. The $u_{0.6}^> - u_{1.2}^>$ residual quadrupole exhibits a rather different pattern, reaching its maximum amplitude at ($l \approx 156^\circ$, $b \approx -74^\circ$). The value of the quadrupole components of 1.2-Jy and PSC_z as well as those of the VELMOD and $u_{0.6}^> - u_{1.2}^>$ quadrupole residuals computed at a distance of 2000 km s^{-1} are shown in Tab. (4). This comparison is at best qualitative since (i) VELMOD quadrupole is computed in real space while both IRAS quadrupoles refer to redshift space instead, and (ii) the smoothing scheme used in WDKS is different from with ours.

7. CONCLUSIONS

We have compared the model velocity and density fields of the PSC_z survey to those derived from the sparser 1.2-Jy sam-

ple in redshift space. Our model predictions are based on the Nusser & Davis (1994) spherical harmonics decomposition technique and assumes Zeld'ovich approximation and linear biasing.

The IRAS overdensity fields are reconstructed with a smoothing proportional to the 1.2-Jy inter-galaxy separation and exhibit the same general features corresponding to the known cosmic structures in the local universe. The model velocity field, computed in the LG frame, has a dipole-like appearance, with galaxies moving away from us toward Perseus-Pisces region and approaching the LG from the opposite direction.

The analysis of the velocity multipoles has revealed a significant discrepancy between the PSC_z and 1.2-Jy velocity monopoles in the range $1800 \lesssim s \lesssim 4000 \text{ km s}^{-1}$ in which PSC_z radial velocities are systematically larger than 1.2-Jy ones, that cannot be explained by uncertainties in the IRAS selection functions or incompleteness of the PSC_z catalog at faint fluxes. Also, the mismatch cannot be ascribed to errors derived from shot-noise and treatment of unobserved areas since both have been accounted for with the help of realistic mock IRAS catalogs and the extensive application of bootstrap resampling techniques to both IRAS datasets.

Both IRAS dipole and quadrupole moments are in good agreement within the sampled volume apart from a small mismatch in the u_{10} , $u_{2,-2}$ and u_{22} quadrupole components beyond $s = 7000 \text{ km s}^{-1}$. The agreement between the dipole moments and their consistency with the velocity dipole computed by BD-

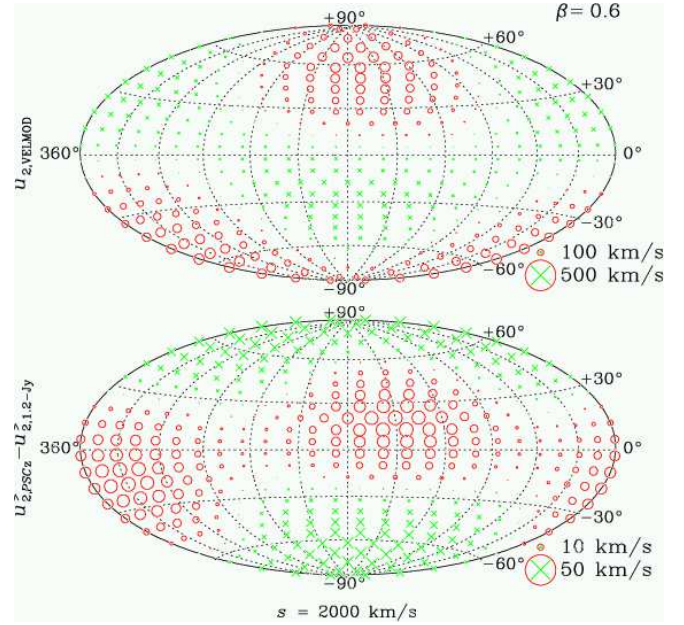


FIG. 15.— VELMOD (upper panel) and $u_{0.6}^> - u_{1.2}^>$ (lower panel) quadrupole residuals at $s = 2000 \text{ km s}^{-1}$. Stars denote outflowing from us (LG frame); circles denote infall to us. The size of the symbol is proportional to the amplitude of the flow (notice the different velocity scales in the two panels). The maximum amplitude of the “VELMOD quadrupole” (top panel) is $\approx 181 \text{ km s}^{-1}$, while for $u_{0.6}^> - u_{1.2}^>$ is $\approx 23 \text{ km s}^{-1}$.

SLS from the ORS catalog suggests that deviations from homogeneous linear biasing prescriptions have to be small and cannot be advocated to explain the aforementioned mismatch between the IRAS monopoles.

Another remarkable consequence of the agreement among the various dipoles is that the 1.2-Jy-*Mark III* residuals cannot be alleviated by using the *PSCz* catalog instead of the 1.2-Jy or the ORS ones. In fact, this suggests that the origin of the 1.2-Jy-*Mark III* dipole resides in the *Mark III* calibration procedure; a suggestion corroborated by the fact that the dipole mismatch disappears when adopting the alternative VELMOD procedure to calibrate -*Mark III* velocities (WDSK). The VELMOD analysis requires a sizable external quadrupole component within 3000 km s⁻¹. This quadrupole accounts for uncertainties errors in the 1.2-Jy model density field beyond that distance. We found that using the *PSCz* sample provides part of the required external tidal field.

As a final remark, we would like to stress that the present analysis illustrates once more the importance of spherical harmonics decomposition techniques to compare observed and model density and velocity fields obtained from all-sky samples, to reveal possible data-model or model-model inconsistencies and to assess model adequacy. These techniques will prove very useful when the next generation of all-sky redshift surveys and peculiar velocity catalogs [e.g. the 6dF (<http://www.mso.anu.edu.au/6dFGS>) and 2MRS (<http://cfa-www.harvard.edu/huchra/2mass>) datasets] will become available.

ACKNOWLEDGEMENTS

We thank Adi Nusser for enlightening discussions. LT was partly funded by FCT (Portugal) under the grants PRAXIS XXI /BPD/16354/98, PRAXIS/C/FIS/13196/98 and POCTI/1999/FIS/36285. LT acknowledges the hospitality of the Aspen Center for Physics and the Kvali Institute for Theoretical Physics where much of the work was completed.

TABLE 4
QUADRUPOLE COMPONENTS AT 2000 km s⁻¹

	VELMOD [km s ⁻¹]	PSCz [km s ⁻¹]	1.2-Jy [km s ⁻¹]	PSCz - 1.2-Jy [km s ⁻¹]
$\mathcal{V}_Q(x,x)...$	45	57	69	-13
$\mathcal{V}_Q(y,y)...$	44	-22	-15	-7
$\mathcal{V}_Q(z,z)...$	-89	-35	-54	20
$\mathcal{V}_Q(x,y)...$	18	-150	-156	6
$\mathcal{V}_Q(x,z)...$	138	57	48	10
$\mathcal{V}_Q(y,z)...$	-29	-106	-102	-5

NOTE.—(1) We have rescaled the “VELMOD quadrupole” components presented in WSDK’s Tab. (2) to the numerical value of $\beta = 0.6$.

REFERENCES

Baker, J. and Davis, M. and Strauss, M. A. and Lahav, O. and Santiago, B., 1999, ApJ, 508, 6
 Branchini, E. and Teodoro, L. and Frenk, C. S. and Schmoldt, I. and Efstathiou, G. and White, S. D. M. and Saunders, W. and Sutherland, W. and Rowan-Robinson, M. and Keeble, O. and Tadros, H. and Maddox, S. and Oliver, S., 1999, MNRAS, 308, 1
 Bunn, E. F., 1995, PhD thesis, University of California, Berkeley
 Canavezes, A. and Springel, V. and Oliver, S. J. and Rowan-Robinson, M. and Keeble, O. and White, S. D. M. and Saunders, W. and Efstathiou, G. and Frenk, C. S. and McMahon, R. G. and Maddox, S. and Sutherland, W. and Tadros, H., 1998, MNRAS, 297, 77
 Cole, S., Weinberg, D. H., Frenk, C. S., and Ratra, B., 1997, MNRAS, 289, 37
 Colless, M. and Dalton, G. and Maddox, S. and Sutherland, W. and Zes Norberg, P. and Cole, S. and Bland-Hawthorn, J. and Bridges, T. and Cannon, R. and Collins, C. and Couch, W. and Cross, N. and Deeley, K. and De Propis, R. and Driver, S. P. and Efstathiou, G. and Ellis, R. S. and Frenk, C. S. and Glazebrook, K. and Jackson, C. and Lahav, O. and Lewis, I. and Lumsden, S. and Madgwick, D. and Peacock, J. A. and Peterson, B. A. and Price, I. and Seaborne, M. and Taylor, K., 2001, MNRAS, 328, 1039
 da Costa, L. N. and Bernardi, M. and Alonso, M. V. and Wegner, G. and Willmer, C. N. A. and Pellegrini, P. S. and Ritte, C. and Maia, M. A. G., 2000, ApJ, 120, 95
 Davis, M. and Nusser, A. and Willick, J., 1996, ApJ, 473, 22
 Dekel, A. and Bertschinger, E. and Yahil, A. and Strauss, M. A. and Davis, M. and Huchra, J. P., 1993, ApJ, 412, 1
 Dekel, A. and Eldar, A. and Kolatt, T. and Yahil, A. and Willick, J. A. and Faber, S. M. and Courteau, S. and Burstein, D., 1999, ApJ, 522, 1
 Eke, V., Cole, S., and Frenk, C., 1996, MNRAS, 282, 263
 Fisher, K. B. and Huchra, J. P. and Strauss, M. A. and Davis, M. and Yahil, A. and Schlegel, D., 1995, ApJS, 100, 69
 Fisher, K. B. and Lahav, O. and Hoffman, Y. and Lynden-Bell, D. and Zaroubi, S., 1995, MNRAS, 272, 219
 Haynes, M. P. and Giovanelli, R. and Salzer, J. J. and Wegner, G. and Freudling, W. and da Costa, L. N. and Herter, T. and Vogt, N. P., 1999, ApJ, 117, 1668
 Hernquist, L. and Katz, N., 1989, ApJS, 70, 419
 Kogut, A., Lineweaver, C., Smoot, G., Banday, C. B. A., N.W.Boggess, Cheng, E., Amici, G. D., Fixsen, D., Hinshaw, G., Jackson, P., Janssen, M., Keegstra, P., Loewenstein, K., Lubin, P., Mahter, J., Tenorio, L., Weiss, R., Wilkinson, D., and Wright, E., 1993, ApJ, 419, 1
 Lahav, O. and Fisher, K. B. and Hoffman, Y. and Scharf, C. A. and Zaroubi, S., Jackson, J., 1999, Classical Electrodynamics, New York: Wiley
 Juszkiewicz, R. and Ferreira, P. G. and Feldman, H. A. and Jaffe, A. H. and Davis, M., 2000, Science, 287, 109
 Nusser, A. and Davis, M., 1994, ApJ, 421, L1
 Nusser, A. and da Costa, L. N. and Branchini, E. and Bernardi, M. and Alonso, M. V. and Wegner, G. and Willmer, C. N. A. and Pellegrini, P. S., 2000, MNRAS, 320, L21
 Rowan-Robinson, M. and Lawrence, A. and Saunders, W. and Crawford, J. and Ellis, R. and Frenk, C. S. and Parry, I. and Xiaoyang, X. and Allington-Smith, J. and Efstathiou, G. and Kaiser, N., 1990, MNRAS, 247, 1
 Saunders, W. and Sutherland, W. J. and Maddox, S. J. and Keeble, O. and Oliver, S. J. and Rowan-Robinson, M. and McMahon, R. G. and Efstathiou, G. P. and Tadros, H. and White, S. D. M. and Frenk, C. S. and Carramíñana, A. and Hawkins, M. R. S., 2000, MNRAS, 317, 55
 Sigad, Y. and Eldar, A. and Dekel, A. and Strauss, M. A. and Yahil, A., 1998, ApJ, 495, 516
 Springel, V., 1996, MSc thesis, Eberhard-Karls-Universität Tübingen
 Strauss, M. A. and Willick, J. A., 1995, PhR, 261, 271
 Zaroubi, S. and Branchini, E. and Hoffman, Y. and da Costa, L. N., 2002, MNRAS, 336, 1234
 Tadros, H., Ballinger, W. E., Taylor, A. N., Heavens, A. F., Efstathiou, G., Saunders, W., Frenk, C. S., Keeble, O., McMahon, R., Maddox, S. J., Oliver, S., Rowan-Robinson, M., Sutherland, W. J., and White, S. D. M.: 1999, MNRAS, 305, 527
 Teodoro, L., 1999, PhD thesis, University of Durham
 Willick, J. and Strauss, M. and Dekel, A. and Kolatt, T., 1997, ApJ, 486, 629
 Willick, J. and Courteau, S. and Faber, S. and Burstein, D. and Dekel, A. and Strauss, M. A., 1997, ApJS, 109, 333
 Willick, J. and Strauss, M. A., 1998, ApJ, 507, 64
 Yahil, A. and Strauss, M. A. and Davis, M. and Huchra, J., 1991, ApJ, 372, 380
 York, D. G. *et al.*, 2000, ApJ, 120, 1579
 Zehavi, I. and Riess, A. G. and Kirshner, R. P. and Dekel, A., 1998, ApJ, 503, 483